RSC Advances

PAPER

View Article Online
View Journal | View Issue

Cite this: *RSC Adv.*, 2021, **11**, 35425

1,4,5,8-Naphthalene tetracarboxylate dianhydride/g-C_3N_4 van der Waals heterojunctions exhibit enhanced photochemical H_2O_2 production and antimicrobial activity†

John H. Thurston,*[a] Molly Vitale-Sullivan,[a] Azhar Koshkimbayeva,[a] Tyler R. Smith[b] and Kenneth A. Cornell[b]

Organic semiconductors, including graphitic carbon nitride (g-C_3N_4, CN), represent an important class of materials for the development of novel antimicrobial or biomedical technologies. Of principal interest is the ability of these materials to catalyze the reduction of elemental oxygen to generate reactive oxygen species (ROS), including hydrogen peroxide (H_2O_2). Here, we describe the fabrication of photoactive van der Waals heterojunctions incorporating 1,4,5,8-naphthalene tetracarboxylic dianhydride (NTCDA) and CN. The composite heterojunction systems were characterized by a combination of physical (TEM, SEM, pXRD), spectroscopic (FT-IR, XPS, DRUV, photoluminescence, TCSPC) and kinetic experiments. Electronic interactions between the two components of the heterojunction increase the rate of photochemical production of H_2O_2 from elemental oxygen by 410%, relative to samples of pure CN. Mechanistic analysis reveals that interaction of NTCDA with the surface of CN modifies the mechanism of H_2O_2 formation in the heterojunction photocatalysts. The photochemical production of H_2O_2 by irradiation of the most active heterojunction composition is sufficient to reduce the viability of *E. coli* O157:H7, *S. aureus* and *Ps. aeruginosa* PAO1 by 99%. Importantly, H_2O_2 production by the NTCDA/CN heterojunctions suppresses *Ps. aeruginosa* biofilm formation, even at light exposure doses that had a lesser impact on overall planktonic cell growth.

Received 8th October 2021
Accepted 25th October 2021

DOI: 10.1039/d1ra07473c

rsc.li/rsc-advances

A. Introduction

Biofilm formation by invasive, pathogenic microorganisms complicates the wound healing process.[1] It has recently been estimated that 65% of microbial infections are associated with biofilm formation.[2,3] Bacteria in biofilm environments express a decreased susceptibility to antimicrobial agents. Therefore, biofilms may act as a unique environmental niche that promotes the recurrence of infections and wound chronicity.[4] In addition, the biofilm environment has been observed to support horizontal gene transfer processes that can facilitate the emergence of antibiotic resistant phenotypes.[2,3,5] Therefore, the development of new technologies to prevent or remediate bacterial biofilm formation is critical for the successful management and control of infection, especially in hospital environments. To this end, it has been reported that an oxidative burst is capable of combatting microbial biofilm formation.[6,7]

Carbon nitride is an intermediate band gap semiconductor that is capable of reacting with elemental oxygen to generate a variety of reactive oxygen species (ROS) including hydrogen peroxide (H_2O_2), super oxide radical anion ($^{\bullet}O_2^-$), singlet oxygen ($^1O_2$) and hydroxyl radical ($^{\bullet}OH$). All ROS are potentially cytotoxic.[8] This photochemical activity has prompted the investigation of carbon nitride and carbon nitride-based materials for a variety of antimicrobial applications, as detailed in several recent review articles.[9,10]

In comparison to activity against planktonic cells, the potential utility of carbon nitride-based materials for preventing or eliminating bacterial biofilms has received significantly less attention. Initial reports illustrated the potential of CN to produce $^1O_2$ (Δ_g), but required extended irradiation to achieve the desired effects.[11,12] Subsequent studies, conducted by both our group and others, have illustrated that CN-mediated ROS formation reduces microbial biofilm formation, but complete inhibition was generally not observed.[13,14]

It is clear that efficient photochemical formation of ROS is critical for developing CN-based systems that effectively combat microbial biofilms. Unfortunately, the photochemical activity of

[a]*Department of Chemistry, The College of Idaho, Caldwell, ID, 83605, USA. E-mail: jthurston@collegeofidaho.edu; Fax: +1-208-459-5175; Tel: +1-208-459-5531*

[b]*Department of Chemistry and Biochemistry, Boise State University, Boise, ID, 83725, USA*

† Electronic supplementary information (ESI) available. See DOI: 10.1039/d1ra07473c

CN can be compromised by high charge carrier recombination rates. This has prompted researchers to explore numerous covalent and noncovalent methods of surface modification to promote the lifetime of photogenerated charge carriers in the CN polymer matrix.[15] Among these approaches, fabrication of van der Waals heterojunctions – in which the two components of the heterojunction are assembled by non-covalent intermolecular interactions – is particularly attractive due to the relative ease of synthesis of these systems and their ability to accommodate a variety of substrates.[16] Consequently, it is reasonable to anticipate that further improvement of the activity of CN-based materials for antibacterial and antibiofilm applications can be realized by developing new van der Waals heterojunctions compositions that support enhanced photochemical ROS formation.

With this goal in mind, we note that the electron affinity of NTCDA ($\chi = 4.1$ eV) is comparable in magnitude to the CN work function ($\Phi = 4.1$–4.3 eV).[17,18] The alignment between the electronic properties of these two materials suggests that interaction of NTCDA with the surface of CN can induce a spontaneous redistribution of electron density, resulting in the formation of an electric field at the heterojunction interface.[19] This electric field is anticipated to promote migration of photogenerated charge carriers and improve the photochemical reactivity of the material for ROS formation.[20]

As part of our group's on going efforts to explore the utility of organic semiconductors for antimicrobial applications, we have fabricated and characterized a series of photoactive NTCDA/CN heterojunctions. Kinetic studies reveal that the composite materials exhibit enhanced H_2O_2 production, while mechanistic analysis indicates that formation of the NTCDA/CN heterojunction induces changes to the oxygen reduction reaction pathway. Antimicrobial screening reveals that the visible light induced H_2O_2 production by the most active NTCDA/CN heterojunction composition reduces the viable population of *E. coli* O157:H7, *S. aureus* and *Ps. aeruginosa*. Importantly, H_2O_2 production by the composite heterojunctions also suppresses biofilm formation by *Ps. aeruginosa*, even at dosage levels that had more modest effects on planktonic cell growth.

B. Experimental

Chemicals and reagents

The reagents urea, 1,4,5,8-naphthalene tetracarboxylic dianhydride (NTCDA), horseradish peroxidase (HRP), *N*,*N*-diethyl-1,4-phenylenediamine sulfate (DPD), nitro blue tetrazolium (NBT), $NaH_2PO_4 \cdot H_2O$, $Na_2HPO_4 \cdot 7H_2O$, hydrogen peroxide (30% aqueous solution), glycerol, toluene, diethyl ether, hexanes and phosphate buffered saline (PBS, 10× concentration) were purchased from Sigma Corporation or Fisher Scientific and used as received without additional purification. Pure strain samples of *E. coli* O157:H7 (ATCC 43894), *S. aureus* (ATCC BAA-44) and *Ps. aeruginosa* PAO1 (ATCC BAA-47) were purchased from ATCC (Manassas, VA). Deionized water (DI H_2O, 18 MΩ) was purified using a Millipore Elix 5 system. Pre-purified nitrogen gas (≥99.99%) was obtained from Norco Corporation (Boise, Idaho). Samples of CN were prepared *via* thermal polymerization of anhydrous urea at 575 °C, as previously described.[21]

Preparation of NTCDA/g-C_3N_4 composite photocatalysts

The desired NTCDA/CN heterojunctions were fabricated by suspending the required amount of solid NTCDA (1 mg, 2.5 mg, 5 mg, 7.5 mg or 10 mg) in 10 mL of anhydrous toluene using a Branson 1510 ultrasonic bath for 30 minutes. The resulting suspension was treated with 100 mg of solid CN and the mixture was again subjected to sonication for an additional 30 minutes. The resulting solid product was collected by filtration using a 30 mL medium porosity Gooch crucible. Successful recovery of both components of the desired vdW heterojunctions was confirmed by assaying the filtrate spectroscopically for dissolved NTCDA ($\varepsilon_{368nm} = 23\ 737\ cm^{-1}$).[22] Under the conditions employed in this study, loss of NTCDA due to solubilization was ≤0.2% of the initial reagent mass across the range of investigated heterojunction sample compositions. The recovered, combined solids were washed with diethyl ether (1 × 15 mL) and hexanes (3 × 15 mL) and dried under reduced pressure before being annealed in air at 150 °C for two hours. The average final yield of the composite samples was >90% in all cases. The final, annealed samples were employed for all subsequent characterization and catalytic testing. Negative control samples were prepared by treating portions of CN as described above without adding NTCDA. The resulting photoactive solids are described with respect to the mass of the NTCDA component present in the heterojunction (*e.g.* 1 mg NTCDA (1N/CN), 5 mg NTCDA (5N/CN) *etc.*).

Characterization

Infrared spectra were collected on a Thermo-Nicolet Avatar 360 FT-IR spectrophotometer. Solution state UV-Vis spectra were collected on a Cary 60 UV/Vis spectrophotometer. Solid state UV-Vis spectra of the semiconducting materials were collected in the range of 250–800 nm on a Cary 5000 UV/Vis spectrophotometer. Steady state photoluminescence and time-correlated single photon counting experiments (TCSPC) were conducted on a Horiba Fluoromax 4 instrument. The TCSPC decay profiles were analyzed using the DAS-6 software package.[23] Intensity average luminescent lifetimes, $\langle\tau\rangle$, were calculated according to the eqn (1).

$$\langle\tau\rangle = \frac{\sum_1^i \tau_i^2 \times \beta_i}{\sum_1^i \tau_i \times \beta_i} \quad (1)$$

Powder X-ray diffraction data was collected on a Rigaku Miniflex 600 powder X-ray diffractometer using Cu K_α radiation (graphite monochromator, $\lambda = 1.5418$ Å). Transmission electron images of g-C_3N_4 were recorded on a Hitachi S-3400N analytical transmission electron microscope operating at an accelerating potential of 120.0 kV. Scanning electron micrographs were collected on a FEI Teneo field emission scanning electron microscope. The samples were not coated prior to

imaging to avoid obscuring changes in structural features as a consequence of heterojunction formation. X-ray photoelectron spectroscopy (XPS) was conducted on a Kratos Analytical XPA Axis Ultra DLD instrument with monochromated Al Kα radiation (1486.6 eV). Binding energies are referenced to adventitious carbon (C 1s: 284.5 eV). Plotting and analysis of all analytical data sets presented in this manuscript was conducted on the software included with the individual instruments or with the Origin 2021 Pro software package.[24]

Sample irradiation procedures

All sample irradiation experiments were carried out using visible radiation (400 nm $\leq \lambda \leq$ 800 nm) provided by a Newport Oriel 300 W ozone free xenon light source, as described previously.[25] Under the operating conditions employed in the course of this study, the average power of the light source at the wavelength of the CN band gap is 98.6 ± 0.2 mW cm^{-2}. Appropriate band pass and cut off filters were employed in all experiments to remove ultraviolet and infrared radiation. In a typical experiment for this study, samples of the target photocatalyst (1 g L^{-1}) were dispersed in 10% glycerol by sonicating for 5 minutes. A 0.5 mL aliquot of the solvent mixture was collected (time = 0 min). The reaction mixture was subjected to visible irradiation and 0.5 mL aliquots were collected at 30, 60, 120 and 180 minutes. Photochemical production of H_2O_2 by composite semiconducting materials was monitored by a modified DPD/HRP spectrophotometric assay.[26,27] Reaction aliquots were diluted with DI H_2O as required (typically 1 : 10) to remain in the linear range of the assay. Apparent quantum yield (AQY) experiments were conducted as described above using a monochromatic light source (λ = 405 nm; 1.5 mJ cm^{-2}) fitted with a Newport PCC lens (KPC043, effective irradiation area = 4.9 cm^2), and applying the calculations as previously detailed by Zeng and coworkers.[28]

Analysis of superoxide formation

Photochemical production of superoxide was assessed using a NBT-based assay.[29,30] In a typical experiment, 5.0 mg of the target photocatalyst was dispersed in 20 mL of a mixture of 20 μM NBT/10% glycerol by sonicating for 5 minutes seconds. The resulting mixture was stirred in the dark for thirty minutes to establish absorption/desorption equilibrium with the surface of the photocatalyst. A 3.0 mL aliquot of the reaction mixture was collected (time = 0 min). The catalyst/NBT reaction mixture was irradiated and 3.0 mL aliquots were collected in 15 minutes intervals for a total of 60 minutes. Residual photocatalyst was removed by passing the reaction aliquots through 0.22 μm PTFE membrane filters. Superoxide formation was indicated by diminution of the NBT absorbance peak at λ = 259 nm. Solutions with known NBT concentrations were employed to create a standard curve for data analysis and the quantity of photolytically generated superoxide was calculated using a 4 : 1 mole-to-mole ratio for reaction with NBT.[29] The NBT concentration employed in the assay was at least a 4-fold molar excess over the superoxide concentration generated in any sample.

Antimicrobial and antibiofilm testing

All assays for antimicrobial and antibiofilm activity by samples of the NTCDA/CN heterojunctions were conducted according to standard protocol.[31,32] Samples of the most active NTCDA/CN composite materials (5N/CN) (1 g L^{-1}) were suspended in a solution comprised of 10% aqueous glycerol and phosphate buffered saline (1× concentration, pH = 7.4) and subjected to visible radiation (400 nm $\leq \lambda \leq$ 800 nm) using the same equipment described in the general procedure above for periods of 0, 1 and 2 hours. Samples of the resulting photochemically generated H_2O_2 solutions were filter sterilized (0.2 μm PTFE filters), stored at 0 °C and employed in antimicrobial experiments within 6 hours of production, as previously described.[13] Bacterial growth was quantified by collecting absorbance readings (λ = 600 nm) after 24 h and 48 h of growth using a Biotek Synergy HT microplate reader. Similarly, biofilm formation by samples of *Ps. aeruginosa* was assessed *via* crystal violet staining.[13] All antimicrobial and antibiofilm studies were repeated twice, with each data point being tested in triplicate. Growth data is represented as the average of the % maximum growth ± standard error of the mean, where the 100% control growth was based on samples that lacked H_2O_2. Biofilm data is similarly graphed as the average of the % maximal biofilm ± standard error of the mean. Data was analyzed using GraphPad Prism 6.0 software.[33] Statistically significant differences between treatment groups were determined by 2-way ANOVA followed by Bonferroni post-hoc tests using GraphPad Prism software, with $p < 0.05$ considered significant.

C. Results & discussion

Characterization

Photoactive composite NTCDA/g-C_3N_4 heterojunctions were successfully fabricated by a direct sonication-mediated synthetic strategy that has recently been employed to produce other CN-based composite materials.[34] The morphology of the developed composite heterojunction materials was directly explored using a combination of transmission electron microscopy (TEM) and scanning electron microscopy (SEM) experiments (Fig. 1). TEM analysis indicates that samples of CN contain highly folded aggregates of discrete carbon nitride polymer sheets. No significant changes in morphology are observed as a consequence of NTCDA deposition, highlighting the stability of the carbon nitride lattice under the conditions required for deposition of NTCDA and formation of the desired photoactive vdW heterojunctions. Complementary SEM analysis reveals an increase in surface roughness as a consequence of NTCDA deposition. This change may be attributed to adsorption of NTCDA crystallites to the CN polymer surface.

Successful deposition of NTCDA on the surface of CN is confirmed by a combination of FT-IR and pXRD experiments. The strongest peaks in the FT-IR spectrum are associated with the tri-*s*-triazine core of the CN polymeric network, in agreement with the ratio of the two individual components employed in the fabrication of the composite samples. Deposition of NTCDA results in progressive emergence of two new peaks

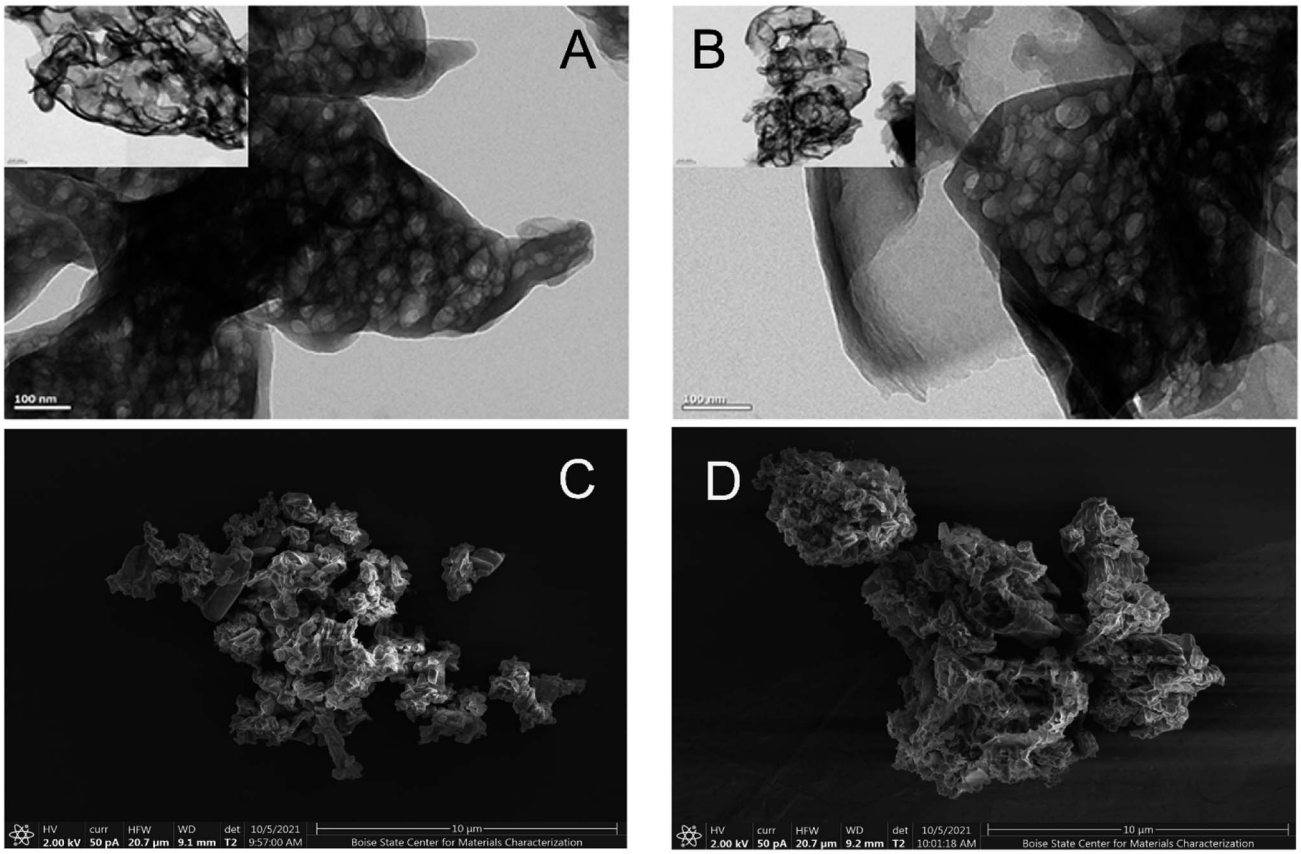

Fig. 1 Representative transmission and scanning electron micrographs detailing the structure and surface morphology observed for samples of pure CN (regions A & C) and the heterojunction composition containing the highest NTCDA loading, 10N/CN (regions B & D). The inset images provide lower magnification views of the same samples depicted in regions A & B (inset scale bars are 0.2 μm).

centered at 1780 cm^{-1} and 1038 cm^{-1} (Fig. 2A). These new peaks are assigned to vibrational modes associated with the carbonyl groups ($\nu_{C=Osym}$ and ν_{C-O-C} + δ_{C-H} + δ_{ring}) of the NTCDA molecular layer, respectively.[35] Both of these peaks are shifted to lower vibrational frequency, relative to pure samples of NTCDA. Such a change in vibrational frequency is indicative of a redistribution of electron density as a consequence of interactions between the two components of the heterojunction.[36]

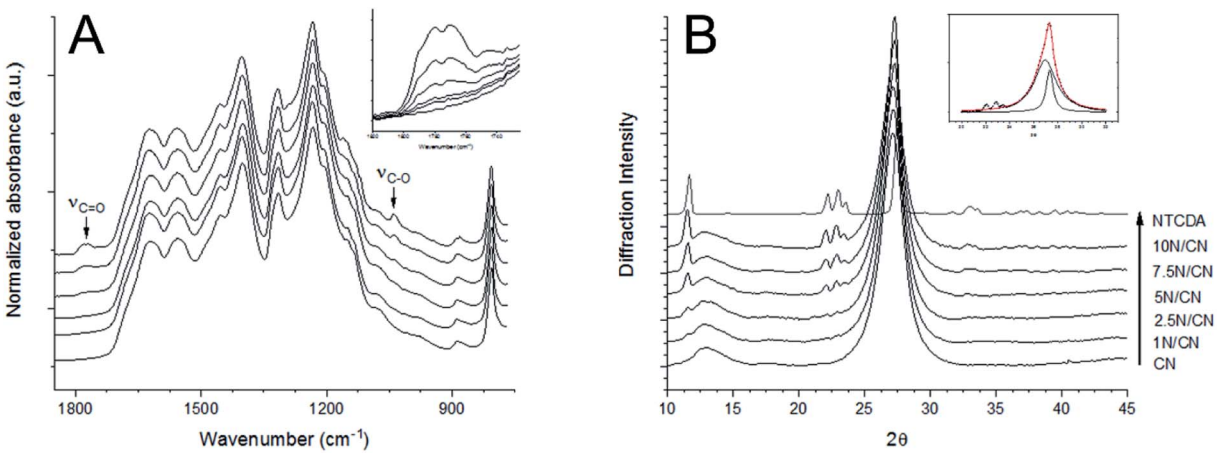

Fig. 2 (A) FT-IR spectra of NTCDA/CN heterojunctions containing different loadings of NTCDA. The inset image highlights the emergence of the $\nu_{C=O}$ vibration with increasing NTCDA content. (B) Powder X-ray diffraction patterns of different NTCDA/CN heterojunction compositions. The inset image details the fitting technique employed to distinguish between the overlapping CN ⟨002⟩ and combined NTCDA ⟨113⟩/⟨013⟩ reflections.

Additional structural detail is provided by X-ray powder diffraction experiments. The diffraction pattern of CN contains two principle reflections, centered at $2\theta = 12.9°$ ($\langle 100 \rangle$, $d = 6.94$ Å) and $2\theta = 27.1°$ ($\langle 002 \rangle$, $d = 3.24$ Å) (Fig. 2B). As with the FT-IR experiments, deposition of NTCDA results in the emergence of new peaks in the pXRD pattern. These new peaks align well with the location and intensity expected for NTCDA crystallites, as determined by comparison to authentic samples. The CN $\langle 002 \rangle$ reflection overlaps with the combined $\langle 113 \rangle$ ($2\theta = 27.4°$, $d = 3.25$ Å) and $\langle 013 \rangle$ ($2\theta = 27.7°$, $d = 3.21$ Å) NTCDA peaks in the diffraction patterns of the NTCDA/CN heterojunctions. This overlap results in an evolution of diffraction peak shape as a function of heterojunction composition. Deconvolution and analysis of these combined peaks indicates a modest migration of the CN $\langle 002 \rangle$ reflection from 27.1° (pure CN) to 26.9° (10N/CN), suggesting a slight expansion of the interplanar spacing of the CN matrix as a consequence of heterojunction formation.

Information about the surface composition and electronic structure of the materials developed for this study is provided by XPS analysis. Survey scans of samples of CN and the representative heterojunction composition 5N/CN reveals both samples to be composed exclusively of carbon, nitrogen and oxygen (ESI, Fig. S1†). As anticipated, deposition of NTCDA increases the amount of carbon and oxygen relative to nitrogen. The C 1s region of the CN XPS spectrum can be deconvoluted to identify three components with binding energies of 287.8 eV (N–C═N), 285.6 eV (sp^3 C–N/C–O) and 284.5 eV (sp^2/sp^3 C–C) (Fig. 3A). Formation of 5N/CN results in a new peak centered at 288.9 eV (O–C═O) as well as an increase in the relative intensity of the sp^2/sp^3 C–C peak. Significantly, the N–C═N peak of the CN polymer matrix shifts to higher binding energy (287.9 eV) upon interaction with NTCDA. The retention of CN matrix peaks in the C 1s XPS spectrum of 5N/CN is consistent with previous reports indicating that surface deposition of NTCDA follows Volmer–Weber growth patterns and likely proceeds *via* formation of discrete adlayer islands.[37]

Similarly, analysis of the O 1s portion of the CN XPS spectrum identifies two components with binding energies of 531.8 eV (C═O) and 533.3 eV (C–O), respectively (Fig. 3B). Deposition of NTCDA to produce 5N/CN causes the C═O peak to shift to the lower binding energy value of 531.5 eV. No change in binding energy is observed for the C–O peak. Shifts in core level XPS binding energies are noted to provide evidence for electronic interactions between the two components of a heterojunction.[38] The C═O peak present in the 5N/CN O 1 s XPS spectrum necessarily derives a majority of its' character from the surface-bound NTCDA component. Consequently, when considered in the context of the complementary shift in binding energy observed in the C 1s region, this data reflects a migration of electron density from the electron rich CN framework to NTCDA.

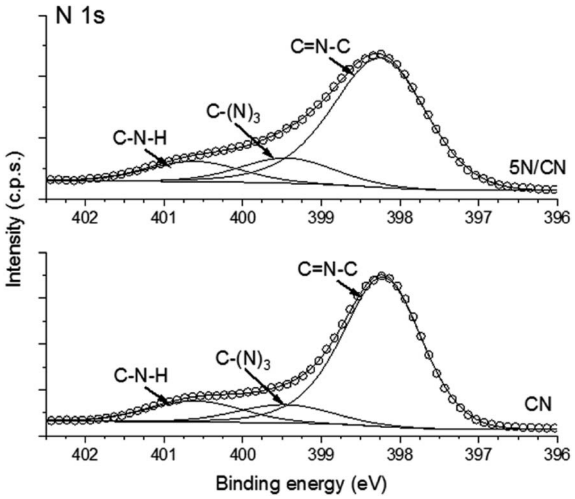

Fig. 4 Comparison of the deconvoluted N 1s region of the core level XPS spectra observed for samples of pure CN and composite heterojunction 5N/CN.

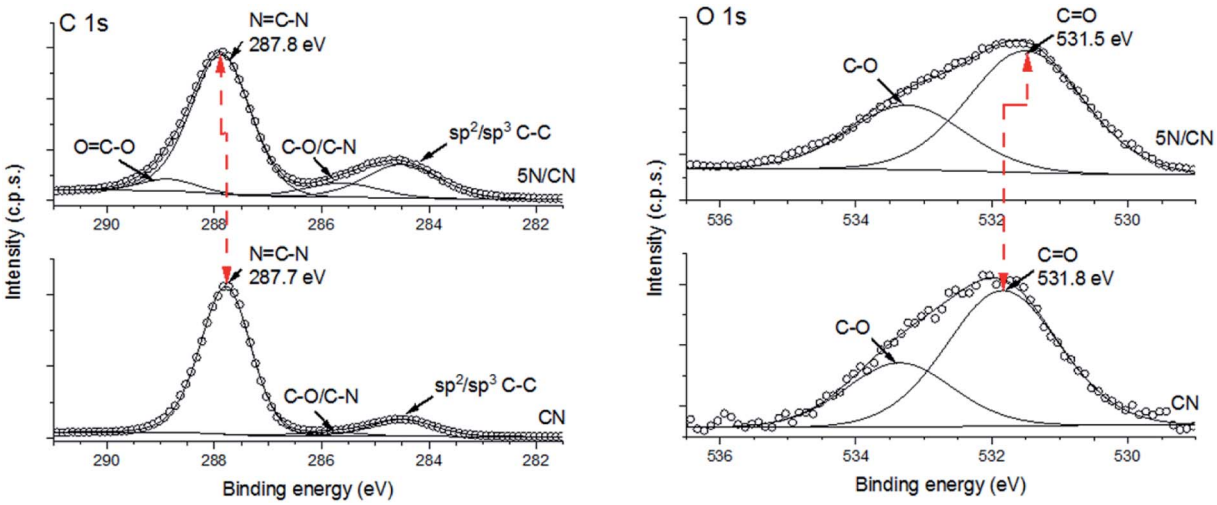

Fig. 3 Comparison of the deconvoluted C 1s and O 1s regions of the core level XPS spectra observed for samples of pure CN and the composite heterojunction 5N/CN. Dashed red vertical lines are presented to highlight shifts in binding energy observed as a consequence of heterojunction formation.

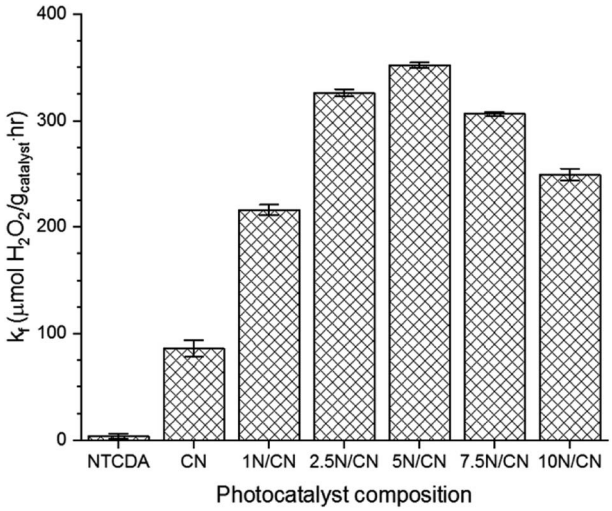

Fig. 5 Comparison of the rate of photochemical formation of H_2O_2 by NTCDA/CN heterojunctions. Control samples of pure CN and pure NTCDA are also presented for comparison. Error bars represent the standard error of the mean (SEM) of two unique trials.

Further context for this analysis is provided by consideration of the N 1 s portion of the XPS core level spectrum (Fig. 4). The N 1s peak of both CN and 5N/CN can be deconvoluted to identify three components with binding energies of 398.2 eV (C=N–C), 399.5 eV (N–$(C)_3$) and 400.6 eV (N–H). In contrast to the changes in binding energy described for C 1s and O 1s, the N 1s core level spectrum of CN is unaffected by interaction with NTCDA. In this case, we note that the valence band of CN derives much of its' character from nitrogen lone pair electrons, while the higher energy conduction band is dominated by carbon p_z orbitals.[39] When considered in total, the presented XPS data are consistent with electronic interaction between the CN conduction band and the lowest unoccupied molecular orbitals (LUMO) of NTCDA. Importantly, no new chemical environments are detected in either the N 1s or the O 1s spectra of the NTCDA/CN heterojunction, indicating that NTCDA successfully self-assembles on the surface of CN to form the desired van der Waals heterojunction, without undergoing condensation with residual amine functional groups.

The structural and electronic modifications described above have the potential to support enhanced orbital overlap and charge transport between the two components of the NTCDA/CN heterojunction, which can promote the photochemical reactivity of the composite materials.[34] Accordingly, the ability of NTCDA/CN heterojunctions to catalyze production of H_2O_2 *via* reduction of elemental oxygen was explored. All of the materials developed in this study, including CN, generate H_2O_2 when subjected to visible radiation (ESI, Fig. S2†). However, H_2O_2 production by NTCDA-containing heterojunctions occurs at an enhanced rate relative to either pure samples of CN or NTCDA alone (Fig. 5). In all cases, the rate of H_2O_2 production for the NTCDA/CN heterojunctions is greater than the sum of the individual rates observed for pure samples of CN and NTCDA, confirming that electronic interactions between these two components enhances the photocatalytic activity of the materials. The highest rate of H_2O_2 production is observed for the heterojunction composition 5N/CN. Samples of 5N/CN exhibit a rate of H_2O_2 formation that is *ca.* 4.1 times higher than pure CN and more than two orders of magnitude higher than pure NTCDA. The subsequent decline in reactivity observed for heterojunction compositions that contain higher NTCDA loadings may be due to either physical occlusion of reactive sites or charge carrier recombination and quenching as a result of long-range conjugation and communication between individual molecules present in the NTCDA layer.[34] Spectroscopic characterization of irradiated heterojunction samples reveals no significant change in structure or functionality, relative to control samples not subjected to visible radiation (ESI, Fig. S3†). Similarly, we were able to the recover and recycle samples of the NTCDA/CN heterojunction photocatalyst three times without a significant change in photochemical activity (ESI, Fig. S4†). These results indicate that, under the conditions of this study, the NTCDA/CN heterojunction photocatalysts are

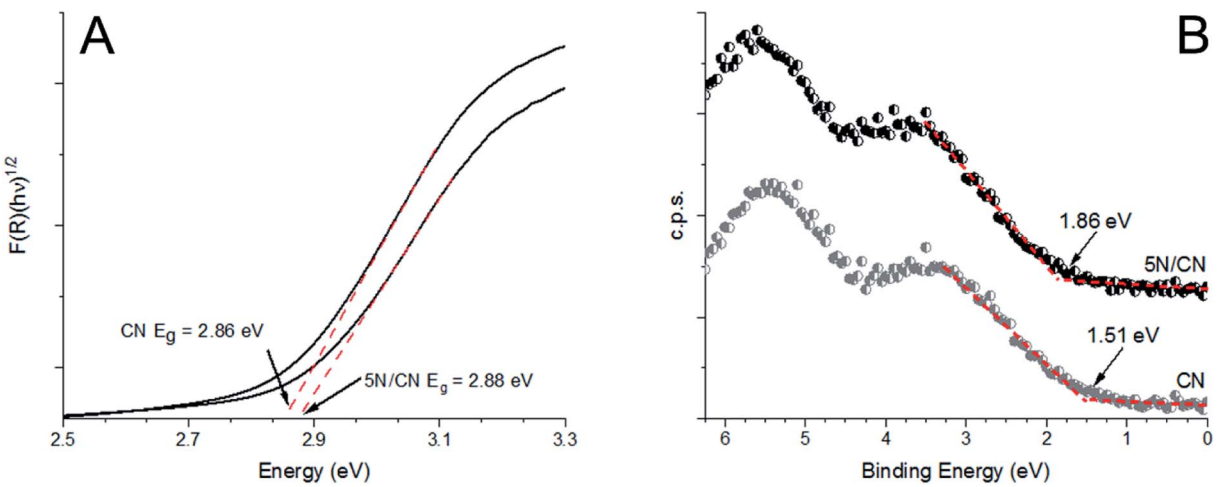

Fig. 6 Tauc plots (A) and valence band XPS spectra (B) observed for samples of CN and the composite heterojunction 5N/CN.

stable against unwanted degradation as a consequence of electronic cycling and photocatalytic H_2O_2 formation.

It is clear that numerous factors, including modification of catalyst surface area, defect sites and electronic structure can contribute to changes in catalytic activity. However, in the case of this investigation, where all photocatalyst samples are derived from a common CN precursor stock, the observed improvements in photochemical reactivity can arise from either (1) the catalyst becoming responsive to a larger fraction of the incident photon flux or (2) improvements in the reactivity of photogenerated charge carriers. Additional insight into the origins of the improved photochemical reactivity of the materials developed in this study is provided by comparison of the AQY for samples of CN and 5N/CN. The AQY of CN is 0.53%. Formation of the 5N/CN heterojunction increases the AQY of the photocatalyst to 1.45%, an increase in photochemical response of 274%. The enhancement of AQY by samples of 5N/CN aligns with the observed improvement in the rate of formation (k_f) of H_2O_2 and indicates that the enhanced reactivity principally arises from interactions between the NTCDA and CN components of the semiconductor heterojunction that promote the reactivity of photogenerated charge carriers. This analysis is consistent with the XPS analysis.

Electronic structure of NTCDA/CN heterojunctions

The enhanced charge carrier behavior indicated by the AQY experiments prompted us to further explore the electronic structure of the NTCDA/CN heterojunctions. Samples of CN possess an indirect band gap of 2.86 eV (Fig. 6A). Deposition of NTCDA on CN to generate the heterojunction 5N/CN results in a modest increase of the semiconductor band gap to 2.88 eV. Similarly, the HOMO–LUMO transition of NTCDA is 3.37 eV, as determined by excitation spectroscopy (ESI, Fig. S5A†). Valence band XPS spectroscopy indicates that the valence band edge of CN sits at a potential of +1.51 V (NHE) (Fig. 6B). The NTCDA HOMO sits at a potential of +3.05 V (NHE), in agreement with previous reports[40] (ESI, Fig. S5B†). Upon interaction with NTCDA, the valence band edge of CN shifts to a potential of +1.86 V (NHE) (Fig. 6B). Given that the semiconductor band gap is only slightly altered on heterojunction formation, this shift in band edge potential is understood to arise from orbital alignment and subsequent redistribution of electron density between the two components of the heterojunction, in agreement with the XPS data. The individual electronic structures of CN and NTCDA are appropriate to produce a type 2 heterojunction. Under the influence of visible radiation, which was the primary focus of this study, only the CN component of the heterojunction is photochemically active, with NTCDA acting to accept and physically sequester photoexcited electrons, prior to reducing oxygen (Fig. 7).

Additional analytical support for this analysis is provided by a combination of steady-state and time-resolved photoluminescence (PL) spectroscopy experiments. Samples of CN produce a broad steady-state PL peak centered at $\lambda = 455$ nm due to radiative recombination of photogenerated charge carriers (Fig. 8). Deposition of 5% NTCDA to fabricate the heterojunction 5N/CN reduces the intensity of the PL peak by *ca.* 20% due to a reduction in the rate of recombination events. Importantly, heterojunction formation results in no significant change in the structure or wavelength maximum of the emission spectrum. This is consistent with the lack of change in the CN band gap, as described above.

Additional insight into charge carrier dynamics in the NTCDA/CN heterojunctions is provided by time correlated single photon counting (TCSPC) experiments (Fig. 9). The luminescent decay curves of samples of CN and 5N/CN were successfully modeled using triexponential kinetics, in agreement with previous reports.[41,42] As illustrated in Table 1, all of the individual lifetime components of the heterojunction 5N/CN are shortened relative to what is observed for equivalent

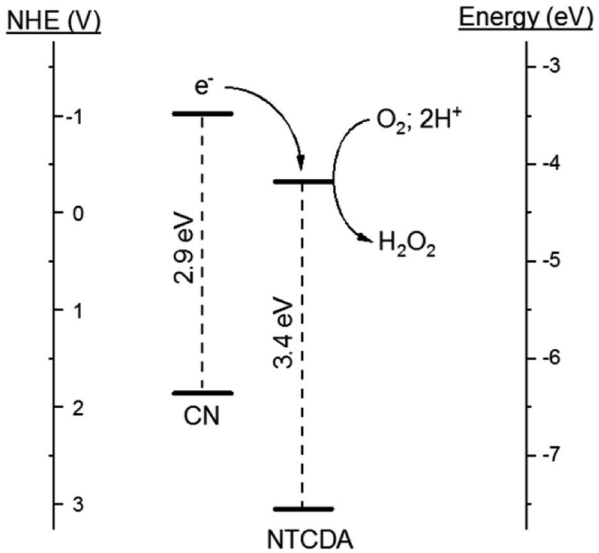

Fig. 7 Proposed electronic alignment of the individual components of the NTCDA/CN heterojunctions.

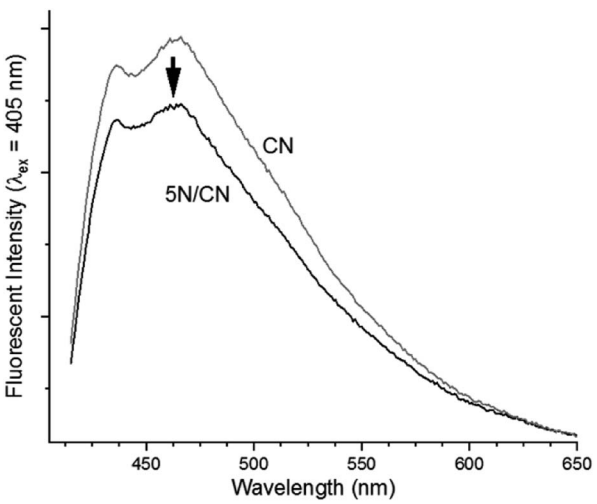

Fig. 8 Comparison of the steady-state photoluminescence behavior of samples of CN and the composite heterojunction 5N/CN.

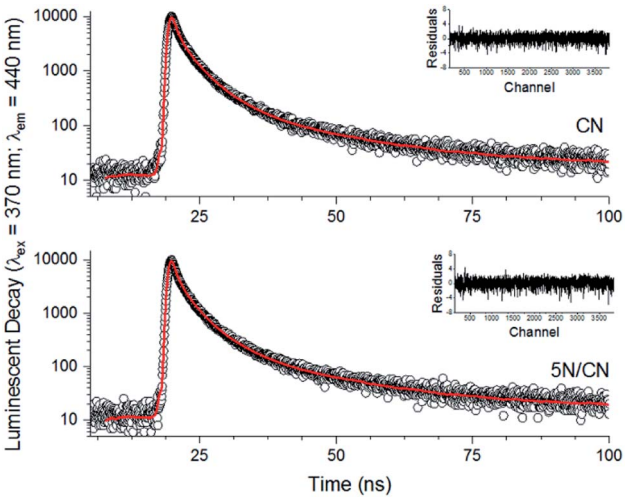

Fig. 9 Comparison of time resolved photoluminescent spectra observed for samples of CN (top) and the heterojunction 5N/CN (bottom). The red line illustrates the results of fitting the experimental data with triexponential kinetics while the inset image provides the residuals from the fitting process. The extracted individual lifetime parameters and the calculated intensity average luminescent lifetime for each sample are provided in Table 1.

samples of CN. Moreover, the decay profile of 5N/CN shifts to favor τ_1 and τ_3 at the expense of τ_2, indicating a modification in the mechanism of charge carrier recombination as a consequence of heterojunction formation. Specifically, the long-lived lifetime component, τ_3, stems from intersystem crossing events that occur between the σ^* and π^* sets of orbitals present in the CN conduction band.[42] Interaction of adsorbed NTCDA molecules with the CN surface effectively extends the conjugated π network of the semiconductor matrix.[36] This extended conjugation reduces the energy difference between the σ^* and π^* orbital sets and facilitates relaxation of charge carriers by this pathway.[42] Importantly, the increased weight of τ_3 in the 5N/CN luminescent decay profile reinforces the results of the XPS analysis discussed above and further highlights the ability of surface adsorbed NTCDA molecules to interact electronically with the CN matrix.

The intensity average luminescent lifetime, $\langle\tau\rangle$, is a convenient method to compare the decay kinetics of different materials.[42] As detailed in Table 1, samples of 5N/CN exhibit a reduced value of $\langle\tau\rangle$, indicative of accelerated decay kinetics, relative to CN. The combined shortening of $\langle\tau\rangle$ and reduction of PL emission intensity for samples of 5N/CN relative to CN indicates increased quenching of radiative processes in the heterojunction semiconductor matrix. This quenching may be attributed to the emergence of competing non-radiative relaxation pathways, including localized trapping of charge carriers by transfer of electron density from CN to surface-bound NTCDA molecules.[43,44] The resulting non-emissive, surface-trapped electrons have the potential to promote the desired oxygen reduction reactions at the photocatalyst surface.[45] The rate of injection of electrons (k_{CT}) from CN to NTCDA was calculated according to eqn (2) and is $6.70 \times 10^7\ s^{-1}$. This value compares extremely favorably to electron transfer rates reported for other CN-based materials.[41,46]

$$k_{(CT)} = \frac{1}{\tau(\text{heterojunction})} - \frac{1}{\tau(\text{g-}C_3N_4)} \quad (2)$$

To experimentally validate the results of the PL and TCSPC analysis described above, we irradiated samples of the 5N/CN heterojunction under an inert atmosphere in the presence of the hole scavenging agent glycerol. Deposition of NTCDA on the surface of CN promotes accumulation of photoelectrons, as illustrated by the formation of a characteristic blue-green color in the irradiated sample[45,47] (ESI, Fig. S6†). In contrast, irradiation of samples of pure CN for equivalent lengths of time and under equivalent reaction conditions does not induce a color change of the photocatalyst sample. Moreover, the blue-green color of the irradiated 5N/CN heterojunction is immediately discharged upon exposure to an ambient atmosphere, indicating that photoexcited electrons in the heterojunction are suitably reducing to react with elemental oxygen. This analysis reinforces the results of the previously described AQY and spectroscopic analysis and confirms that interaction of NTCDA with the surface of CN is promotes the reactivity of photoexcited electrons and supports the desired oxygen reduction reactions.

Influence of NTCDA/CN heterojunction formation on mechanism of H_2O_2 production

As illustrated in Scheme 1, reduction of elemental oxygen to generate H_2O_2 can occur by multiple mechanistic pathways. We explored how heterojunction formation influences the

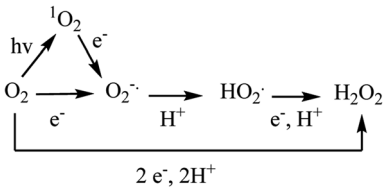

Scheme 1 Possible reaction pathways for formation of H_2O_2 from elemental oxygen.

Table 1 Comparison of TCSPC kinetic data (λ_{ex} = 370 nm; λ_{em} = 440 nm) for samples of CN and the composite heterojunction 5N/CN

Sample	τ_1 (%)	τ_2 (%)	τ_3 (%)	$\langle\tau\rangle$	χ^2
CN	0.70 ns (30.96%)	2.02 ns (61.96%)	19.64 ns (7.10%)	2.86 ns	1.10
5N/CN	0.63 ns (31.98%)	1.85 ns (60.45%)	14.36 ns (7.54%)	2.40 ns	1.16

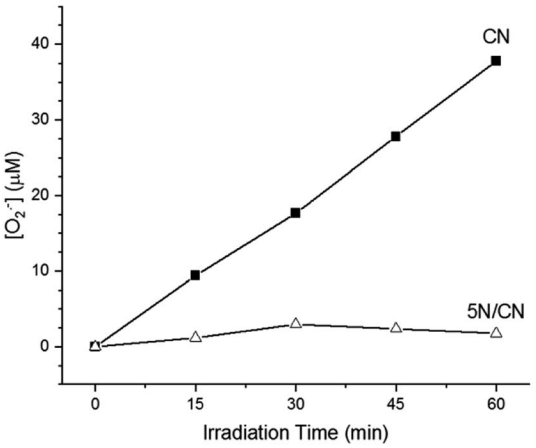

Fig. 10 Comparison of photochemical production of the superoxide radical ion by samples of CN and the composite heterojunction 5N/CN.

mechanism of O_2 reduction by assessing how superoxide radical anion production is influenced by photocatalyst composition. Visible light irradiation of CN produces superoxide in a linear fashion for the duration of the reaction period (Fig. 10). The total quantity of superoxide generated in this experiment (*ca.* 5.6 μmol) closely matches the total quantity of H_2O_2 produced by the catalyst under similar irradiation conditions (*ca.* 5.5 μmol). The correlation in these quantities indicates that, under the conditions employed in this study, photochemical production of H_2O_2 by samples of CN occurs predominately *via* a superoxide-mediated mechanistic pathway. In contrast, irradiation of 5N/CN results in no detectable production of superoxide, even as the rate of H_2O_2 formation increases by a factor of >4. The difference in the activity of these two materials suggests that deposition of NTCDA on the surface of CN serves to both enhance the photochemical reactivity of the material as well as modify the mechanism of the oxygen reduction reaction itself. The ability of conjugated organic molecules that contain two or more carbonyl groups to support photochemical reduction of elemental O_2 has been described in the literature.[48] Further, transfer of electron density from CN to NTCDA, as suggested by the spectroscopic data described above, could result in the formation of a transient partially reduced (*leuco*) species.[49] Such *leuco* complexes have been previously invoked as reactive intermediates that are able to activate elemental oxygen for subsequent conversion to H_2O_2.[50,51]

Antimicrobial and antibiofilm activity of NTCDA/CN heterojunctions

The enhanced photochemical production of H_2O_2 by NTCDA/CN composite heterojunctions indicates that these materials have the potential to function as viable agents for antimicrobial applications. Accordingly, H_2O_2 was generated by irradiating the most active heterojunction composition (5N/CN) for period of either 1 or 2 hours. Portions of the resulting H_2O_2-containing solutions were administered to samples of *E. coli* O157:H7, *S. aureus* and *Ps. aeruginosa* PAO1. The ROS-containing aliquots induced a dose-related response in the microbial samples that was proportional to the length of irradiation of the heterojunction photocatalyst and the corresponding solution H_2O_2 concentration. As illustrated in Fig. 11A, administration of photogenerated H_2O_2 (2 hours irradiation) to *S. aureus* (Gram

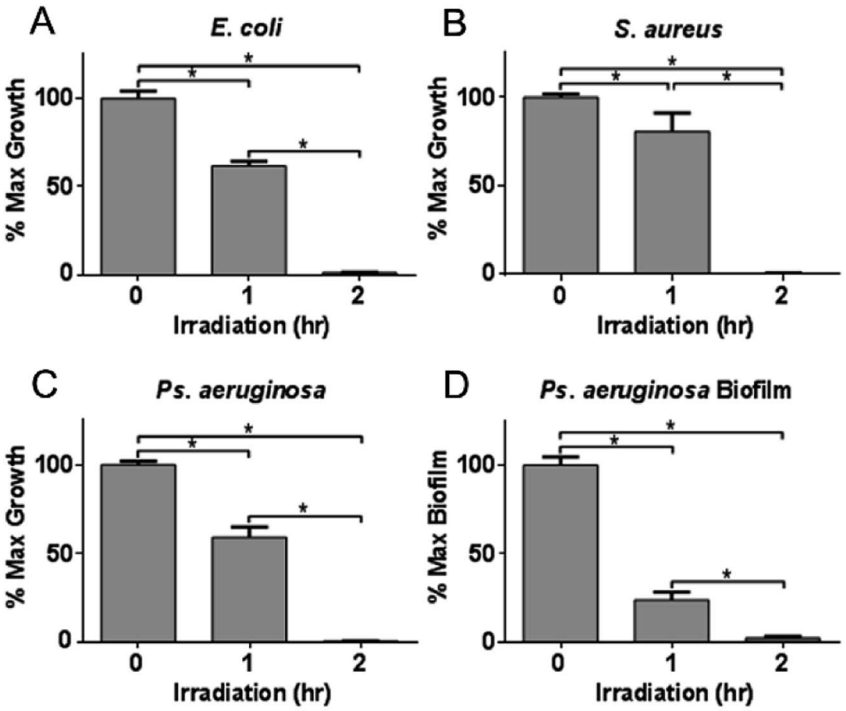

Fig. 11 Observed inhibition of bacterial growth (charts A–C) and biofilm formation (chart D) as a consequence of photogenerated H_2O_2-produced by irradiation of samples of 5N/CN. Error bars are SEM, $N = 6$, * indicates $p < 0.001$.

positive coccus) results in $a > 99.4\%$ decline in total microbial viability. Similar biocidal effects were achieved in studies employing *E. coli* O157:H7 (98.8% reduction in viability) and *Ps. aeruginosa* PAO1 (>99%) (Fig. 11B and C).

We further assessed the effect of photogenerated H_2O_2 on microbial biofilm formation. Administration of H_2O_2 produced by 1 hour irradiation of 5N/CN to *Ps. aeruginosa* PAO1 results in a $76.3 \pm 4.2\%$ decline in biofilm formation, even as the total viability of the target organism (as measured by culture density) is reduced by a more modest $40.9 \pm 5.2\%$ (Fig. 11D). The decline in biofilm formation in *Ps. aeruginosa* PAO1 suggests that the photogenerated H_2O_2 flux both compromises the physical integrity of the extracellular polysaccharide matrix of the biofilm and reduces the viability of the microorganism itself, resulting in lower adherence of cells in the early stages of biofilm development.[7,52] Importantly, by compromising biofilm formation, the results of this analysis reveal that photogenerated H_2O_2 from NTCDA/CN heterojunctions are able to induce positive biomedical outcomes, even at dosing levels that are not sufficient to effect complete inactivation of the microorganism. Consequently, the results of this study illustrate the potential utility of CN-based materials, including the heterojunctions developed for this study, to function as both novel antimicrobial agents as well as adjunctive therapies to assist in suppressing biofilm formation while other, traditional treatment modalities are employed to combat infections by pathogenic organisms.

D. Conclusions

In this study, NTCDA/CN composite heterojunctions were generated by a direct sonication-mediated synthetic approach. The materials were analyzed by standard physical and spectroscopic techniques. Electronic interactions between the two components of the heterojunction serve to promote transfer of photoexcited electrons from the CN semiconductor to the surface adsorbed NTCDA. This transfer of electron density reduces photogenerated charge carrier recombination events and facilitates the activity of the heterojunctions for oxygen reduction reactions. Consequently, the NTCDA/CN heterojunctions exhibit enhanced activity for formation of H_2O_2 from elemental oxygen, relative to pure samples of either NTCDA or CN. Photochemical production of H_2O_2 by the NTCDA/CN van der Waals heterojunctions reduces the viability of planktonic samples of *E. coli* O157:H7, *S. aureus* and *Ps. aeruginosa* PAO1. Most significantly, H_2O_2 production by 5N/CN successfully suppresses *Ps. aeruginosa* biofilm formation. The results of this study reinforce the potential utility of CN-based materials to function as both antimicrobial agents as well as novel adjunctive therapies that enhance or expand the utility of other, established antimicrobial treatments.

Author contributions

John H. Thurston: conceptualization and writing – original draft. Molly Vitale-Sullivan: investigation. Tyler R. Smith: investigation. Azhar Koshkimbayeva: investigation. Kenneth A. Cornell: methodology and writing – review & editing.

Conflicts of interest

There are no conflicts to declare.

Acknowledgements

The work described in this publication was made possible by Institutional Development Awards (IDeA) from the National Institute of General Medical Sciences of the National Institutes of Health under Grants #P20GM103408 and P20GM109095. JHT and KAC received support from NIH grant R15GM125065, and acknowledge support from the Biomolecular Research Center (RRID:SCR_019174) at Boise State with funding from the National Science Foundation (Grants # 0619793 and #0923535). JHT received additional support from the MJ Murdock Charitable Trust (SR-201811723) and the NASA Idaho Space Grant Consortium (NISGC, Grant #80NSSC20M0108). The authors gratefully acknowledge Prof. Daniel Fologea (Boise State University) for assistance with DRUV experiments and the University of Utah Nanofab facility for assistance with XPS analysis. Powder X-ray diffraction, transmission electron microscopy and scanning electron microscopy experiments were carried out at the Boise State Center for Materials Characterization (BSCMC).

References

1 D. G. Metcalf and P. G. Bowler, *Burns Trauma*, 2013, **1**, 2321–3868.11332.
2 T. F. Mah and G. A. O'Toole, *Trends Microbiol.*, 2001, **9**, 34–39.
3 P. S. Stewart and J. W. Costerton, *Lancet.*, 2001, **358**, 135–138.
4 R. D. Wolcott, D. D. Rhoads, M. E. Bennett, B. M. Wolcott, L. Gogokhia, J. W. Costerton and S. E. Dowd, *J Wound Care*, 2010, **19**, 45–53.
5 K. Abe, N. Nomura and S. Suzuki, *FEMS Microbiol. Ecol.*, 2020, **96**, fiaa031.
6 S. T. Sultana, E. Atci, J. T. Babauta, A. Mohamed Falghoush, K. R. Snekvik, D. R. Call and H. Beyenal, *Sci. Rep.*, 2015, **5**, 14908.
7 Y. S. Raval, A. Mohamed, J. Song, K. E. Greenwood-Quaintance, H. Beyenal and R. Patel, *Antimicrob. Agents Chemother.*, 2020, **64**, e02332-19.
8 F. Vatansever, W. C. M. A. de Melo, P. Avci, D. Vecchio, M. Sadasivam, A. Gupta, R. Chandran, M. Karimi, N. A. Parizotto, R. Yin, G. P. Tegos and M. R. Hamblin, *FEMS Microbiol. Rev.*, 2013, **37**, 955–989.
9 C. Zhang, Y. Li, D. Shuai, Y. Shen, W. Xiong and L. Wang, *Chemosphere*, 2019, **214**, 462–479.
10 G. Liao, F. He, Q. Li, L. Zhong, R. Zhao, H. Che, H. Gao and B. Fang, *Prog Mater Sci*, 2020, **112**, 100666.
11 H. Shen, E. A. López-Guerra, R. Zhu, T. Diba, Q. Zheng, S. D. Solares, J. M. Zara, D. Shuai and Y. Shen, *ACS Appl. Mater. Interfaces*, 2019, **11**, 373–384.

12 H. Shen, D. P. Durkin, A. Aiello, T. Diba, J. Lafleur, J. M. Zara, Y. Shen and D. Shuai, *J. Hazard. Mater.*, 2021, **408**, 124890.
13 J. H. Thurston, A. J. Clifford, B. S. Henderson, T. R. Smith, D. Quintana, K. F. Cudworth, T. J. Lujan and K. A. Cornell, *ACS Appl Bio Mater*, 2020, **3**, 1681–1689.
14 Y.-R. Lin, G. V. C. Dizon, K. Yamada, C.-Y. Liu, A. Venault, H.-Y. Lin, M. Yoshida and C. Hu, *J. Colloid Interface Sci.*, 2020, **567**, 202–212.
15 M. Majdoub, Z. Anfar and A. Amedlous, *ACS Nano*, 2020, **14**, 12390–12469.
16 V. Georgakilas, J. N. Tiwari, K. C. Kemp, J. A. Perman, A. B. Bourlinos, K. S. Kim and R. Zboril, *Chem. Rev.*, 2016, **116**, 5464–5519.
17 S. A. Pshenichnyuk and A. S. Komolov, *J. Phys. Chem. A*, 2012, **116**, 761–766.
18 T. V. M. Sreekanth, P. C. Nagajyothi, G. R. Dillip and Y. R. Lee, *J. Phys. Chem. C*, 2017, **121**, 25229–25242.
19 S.-h. Chen, J.-j. Wang, J. Hunag and Q.-x. Li, *Chin. J. Chem. Phys.*, 2017, **30**, 36–42.
20 B. Zhu, L. Zhang, B. Cheng and J. Yu, *Appl. Catal., B*, 2018, **224**, 983–999.
21 J. H. Thurston, N. M. Hunter, L. J. Wayment and K. A. Cornell, *J. Colloid Interface Sci.*, 2017, **505**, 910–918.
22 T. C. Barros, I. M. Cuccovia, J. P. S. Farah, J. C. Masini, H. Chaimovich and M. J. Politi, *Org. Biomol. Chem.*, 2006, **4**, 71–82.
23 *Decay Analysis Software (DAS), 6.8.16*, Horiba Scientific.
24 *Origin (Pro), Version 2021*, OriginLab Corporation, Northampton, MA, USA.
25 J. H. Thurston, N. M. Hunter and K. Cornell, *RSC Adv.*, 2016, **6**, 42240–42248.
26 G.-H. Moon, M. Fujitsuka, S. Kim, T. Majima, X. Wang and W. Choi, *ACS Catal.*, 2017, **7**, 2886–2895.
27 G.-H. Moon, W. Kim, A. D. Bokare, N.-e. Sung and W. Choi, *Energy Environ. Sci.*, 2014, **7**, 4023–4028.
28 X. Zeng, Y. Liu, Y. Kang, Q. Li, Y. Xia, Y. Zhu, H. Hou, M. H. Uddin, T. R. Gengenbach, D. Xia, C. Sun, D. T. McCarthy, A. Deletic, J. Yu and X. Zhang, *ACS Catal.*, 2020, **10**, 3697–3706.
29 S. Zhao, T. Guo, X. Li, T. Xu, B. Yang and X. Zhao, *Appl. Catal., B*, 2018, **224**, 725–732.
30 L. Yang, G. Dong, D. L. Jacobs, Y. Wang, L. Zang and C. Wang, *J. Catal.*, 2017, **352**, 274–281.
31 NCCLS, *Methods for Dilution Antimicrobial Susceptibility Tests for Bacteria that Grow Aerobically; Approved Standard-Ninth Edition*, National Committee on Clinical Laboratory Standards, 940 West Valley Road, Suite 1400, Wayne, Pennsylvania 19087 USA, 2012.
32 J. H. Merritt, D. E. Kadouri and G. A. O'Toole, *Curr. Protoc. Microbiol.*, 2005, 1B.
33 *GraphPad Prism version 6.0*, GraphPad Software, San Diego, California USA.
34 Q. Gao, J. Xu, Z. Wang and Y. Zhu, *Appl. Catal., B*, 2020, **271**, 118933.
35 H. Abdel-Khalek, E. Shalaan, M. A. El Salam, A. M. El-Sagheer and A. M. El-Mahalawy, *J. Mol. Struct.*, 2019, **1178**, 408–419.
36 Y. Wang, J. Zhou, X. Hao, Y. Wang and Z. Zou, *Appl. Surf. Sci.*, 2018, **456**, 861–870.
37 T. Meisel, M. Sparenberg, M. Gawek, S. Sadofev, B. Kobin, L. Grubert, S. Hecht, E. List-Kratochvil and S. Blumstengel, *J. Phys. Chem. C*, 2018, **122**, 12913–12919.
38 R. Otero, A. L. Vázquez de Parga and J. M. Gallego, *Surf. Sci. Rep.*, 2017, **72**, 105–145.
39 X. Wang, K. Maeda, A. Thomas, K. Takanabe, G. Xin, J. M. Carlsson, K. Domen and M. Antonietti, *Nat. Mater.*, 2009, **8**, 76–80.
40 P. I. Djurovich, E. I. Mayo, S. R. Forrest and M. E. Thompson, *Org. Electron.*, 2009, **10**, 515–520.
41 W.-J. Ong, L. K. Putri, Y.-C. Tan, L.-L. Tan, N. Li, Y. H. Ng, X. Wen and S.-P. Chai, *Nano Res.*, 2017, **10**, 1673–1696.
42 P. Kumar, E. Vahidzadeh, U. K. Thakur, P. Kar, K. M. Alam, A. Goswami, N. Mahdi, K. Cui, G. M. Bernard, V. K. Michaelis and K. Shankar, *J. Am. Chem. Soc.*, 2019, **141**, 5415–5436.
43 X. Ma, X. Li, M. Li, X. Ma, L. Yu and Y. Dai, *Appl. Surf. Sci.*, 2017, **414**, 124–130.
44 Q. Cai, Z. Hu, Q. Zhang, B. Li and Z. Shen, *Appl. Surf. Sci.*, 2017, **403**, 151–158.
45 Y. Zhao, P. Zhang, Z. Yang, L. Li, J. Gao, S. Chen, T. Xie, C. Diao, S. Xi, B. Xiao, C. Hu and W. Choi, *Nat. Commun.*, 2021, **12**, 3701.
46 Z. Zhang, K. Liu, Z. Feng, Y. Bao and B. Dong, *Sci. Rep.*, 2016, **6**, 19221.
47 W. Yang, R. Godin, H. Kasap, B. Moss, Y. Dong, S. A. J. Hillman, L. Steier, E. Reisner and J. R. Durrant, *J. Am. Chem. Soc.*, 2019, **141**, 11219–11229.
48 M. K. Węcławski, M. Jakešová, M. Charyton, N. Demitri, B. Koszarna, K. Oppelt, S. Sariciftci, D. T. Gryko and E. D. Głowacki, *J. Mater. Chem. A*, 2017, **5**, 20780–20788.
49 E. Rostami-Tapeh-Esmail, M. Golshan, M. Salami-Kalajahi and H. Roghani-Mamaqani, *Dyes Pigm.*, 2020, **180**, 108488.
50 T. Kamachi, T. Ogata, E. Mori, K. Iura, N. Okuda, M. Nagata and K. Yoshizawa, *J. Phys. Chem. C*, 2015, **119**, 8748–8754.
51 N. Kaynan, B. A. Berke, O. Hazut and R. Yerushalmi, *J. Mater. Chem. A*, 2014, **2**, 13822–13826.
52 B. E. Christensen, H. N. Trønnes, K. Vollan, O. Smidsrød and R. Bakke, *Biofouling*, 1990, **2**, 165–175.